Solar Energy 220 (2021) 722–734

Contents lists available at ScienceDirect

Solar Energy

journal homepage: www.elsevier.com/locate/solener

Design, development and characterisation of a Building Integrated Concentrating Photovoltaic (BICPV) smart window system

Xiao Liu, Yupeng Wu *

Department of Architecture and Built Environment, Faculty of Engineering, The University of Nottingham, University Park, Nottingham NG7 2RD, United Kingdom

ARTICLE INFO

Keywords:
Building Integrated Concentrating Photovoltaic (BICPV)
Thermotropic membrane
Ray-tracing
Optical concentration ratio

ABSTRACT

Building Integrated Concentrating Photovoltaic (BICPV) window represents a promising alternative approach for improving the electricity generation of photovoltaic cells when integrated into building windows. As a new concept, BICPV smart window consisting of an optically switchable thermotropic layer with integrated PV cells offers the potential to simultaneously generate electricity and control solar heat and visible light into buildings. In this study, a BICPV smart window system with a Hydroxypropyl Cellulose (HPC) based thermotropic hydrogel membrane has been developed and characterised. The system was designed with the aid of a validated wavelength-dependent optical model based on a Monte-Carlo ray-tracing technique, where the thermal and optical properties of the thermotropic layer used for the optical model prediction were obtained from experimental measurement. Subsequently, a prototype of the BICPV smart window system has been fabricated and characterised under controlled indoor conditions. From the experiments, it was found that the maximum power output of the BICPV smart window (6 wt% HPC) increases by 17.1% with the membrane temperature increasing from 40 °C (the transition temperature) to 54 °C; meanwhile, a 70.9% reduction in the light transmittance is observed. This indicated that the BICPC smart window might potentially reduce the solar heat gain in hot periods and therefore reduce the building energy demand. In addition, the effect of different concentrations of HPC polymer (2, 4 and 6 wt%) on the electrical and optical performance of the system has been investigated.

1. Introduction

Global concerns over climate change and ever-increasing energy demand have led to a growing interest in developing renewable energy technologies. Photovoltaic (PV) cells that utilise solar energy for electricity generation have progressed significantly in recent decades (Ogbomo et al., 2017). Integrating photovoltaics into building transparent façade has been increasingly seen in modern building designs (Baig et al., 2014). In such system, photovoltaic cells serve as a part of the transparent building envelope element such as window, glazed façade or skylight, offering savings in materials and generating renewable electricity on-site while reducing excess solar heat and daylight into the indoor spaces (Norton et al., 2011; Skandalos and Karamanis, 2015; Agathokleous and Kalogirou, 2016).

One of the main challenges for wide adoption of BIPV glazing is the optimisation of both daylighting and electricity generation (Hee et al., 2015), which are related to the transparency and power conversion efficiency of selected PV cells. Semi-transparent photovoltaic cells such as amorphous silicon (a-Si) and Dye Sensitised Solar Cell (DSSC) are popular choices for window integration, as they can be manufactured in various degrees of transparency and offer more homogeneous daylighting of the indoor spaces compared to crystalline-silicon (c-Si) solar cells (Skandalos and Karamanis, 2015). In recent years, a growing number of researches have been conducted to investigate the potential use of Building Integrated Concentrating Photovoltaics (BICPVs) to improve the electricity generation, daylighting control and aesthetics of BIPV windows/facades. Sellami and Mallick (2013) presented a Square-Elliptical-Hyperboloid (SEH) shaped static solar concentrator for window integrated concentrating photovoltaics. It was reported that the SEH system with a geometric concentration ratio of 4× achieved an optical efficiency of 68%. Sarmah et al. (2014) developed a semi-transparent Dielectric Asymmetric Compound Parabolic Concentrator (DiACPC) with a geometric concentration ratio of 2.8× with a maximum optical efficiency of 80.5%. In the follow-up research (Sarmah and Mallick, 2015), a 30 cm × 30 cm prototype for the DiACPC based BICPV façade was fabricated and evaluated under outdoor conditions in Edinburgh. The maximum power output of the BICPV façade prototype was found to be 2.27 times higher compared to its non-concentrating

* Corresponding author.
E-mail address: Yupeng.Wu@nottingham.ac.uk (Y. Wu).

https://doi.org/10.1016/j.solener.2021.03.037
Received 10 November 2020; Received in revised form 10 February 2021; Accepted 15 March 2021
Available online 15 April 2021

counterpart under a solar irradiance of 943 W/m^2. Sabry (2016) proposed a BICPV glazed façade using Total Internal Reflection (TIR) prismatic segments that collect most of the direct incident radiation for electricity generation in summer, while allowing the sunlight at lower incidence angles to be transmitted into the building interior for heating in winter. Corrado et al. (2013) developed a 31.8 cm × 31.8 cm Luminescent Solar Concentrator (LSC) window using front-facing solar cells with a PV cell coverage ratio of 31%. The LSC window achieved an overall module efficiency of 6.2% and a power ratio of 1.6 over the counterpart with no LSC during outdoor experimental tests. Wu et al. (2016) introduced the concept and design of a BICPV smart window system with an optically switchable thermotropic layer for electricity generation and passive solar radiation control. 3D ray-tracing simulations have been used to investigate the effects of different membrane reflectances, geometrical concentration ratios, glass cover thicknesses and glass refractive indices on the optical efficiency and optical concentration ratio of the proposed system. Nevertheless, neither prototype has been developed, nor experiment has been conducted to prove the concept and validate the numerical model.

In this research, a novel BICPV smart window system that can generate electricity on-site and also modulate its solar energy transmission in response to thermal stimulus has been designed and developed. The BICPV smart window system consists of solar cells and a Hydroxypropyl cellulose (HPC) based thermotropic membrane layer. A wavelength-dependent Monte-Carlo ray-tracing model has been developed and validated to predict the dynamic behaviour of the novel window system and also in aid of the system design. A prototype of the BICPV smart window system was subsequently fabricated and comprehensively investigated under controlled indoor conditions, in terms of the electrical and optical performance under various membrane temperatures, incident light intensities, incident light angles as well as HPC concentration ratios for the thermotropic membrane layer.

2. Concept of BICPV smart window system

The BICPV smart window system is mainly comprised of a front glass pane, an encapsulation layer with evenly spaced c-Si solar cells, a thermotropic layer and a back glass pane, as shown in Fig. 1. The thermotropic layer switches from a transparent state to a translucent/scattering state when its temperature increases from below a designed temperature threshold (transition temperature) to above it. In other words, when below the transition temperature, the window appears transparent; a portion of the incident solar radiation strikes the solar cells for electricity generation, while most of the rest radiation passes through the window for indoor space heating and daylighting, with a small amount lost due to the reflection off the front glass pane. When the thermotropic layer is in the translucent state, as shown in Fig. 1, a fraction of the scattered radiation is trapped within the window and redirected to the solar cells for electricity generation through Total Internal Reflection (TIR). Some of the scattered radiation escapes from the front and back glass panes because the angles of incidence at the glass-air interface are less than the critical angle expressed by Eq. (1). As heated to a higher temperature, the thermotropic layer becomes increasingly reflective, potentially resulting in higher electricity generation. Meanwhile, less solar heat and light penetrate through the window into the building interior, potentially reducing the risks of overheating and glare.

$$\theta_c = \sin^{-1}\frac{n_{air}}{n_{glass}} \tag{1}$$

where θ_c is the critical angle at the glass-air interface, n_{air} is the refractive index of air and n_{glass} is the refractive index of the glass pane.

3. Methodology

To show the effectiveness of the proposed concept, a small-scale prototype system was developed and evaluated. The system development process applied a series of steps combing experiments and optical simulation (see Fig. 2). Initially, a HPC-based thermotropic hydrogel membrane was synthesised and characterised by optical spectroscopy. The temperature variation of the spectral transmittance and reflectance of the thermotropic hydrogel membrane was measured and then imported to a validated optical model for the design of the prototype system. The optical model was established based on a wavelength-dependent Monte-Carlo ray-tracing technique, which was validated in advanced by experimental tests with commercially available solar control films with different static optical properties (i.e. different films with static transmittances and reflectances). With the aid of the optical model, the prototype system was designed, optimised and fabricated. Finally, indoor experiments were carried out to obtain the prototype system performance and verify the proposed concept.

3.1. Development and characterisation of the thermotropic membrane

3.1.1. Material selection and thermotropic hydrogel synthesis

To fit for window application, thermotropic materials would need to fulfil requirements of Allen et al., 2017, Schneider and Seeboth, 2001, Resch and Wallner, 2009 and Connelly et al., 2017: (1) reversible switching between a clear state with >85% transmittance and a light-scattering state with <15% transmittance; (2) steep switching gradient within a small temperature range (<10 °C); (3) transition temperature in the range between 25 °C and 40 °C; (4) low hysteresis upon heating and cooling; (5) long-term stability and good weatherability; (6) availability

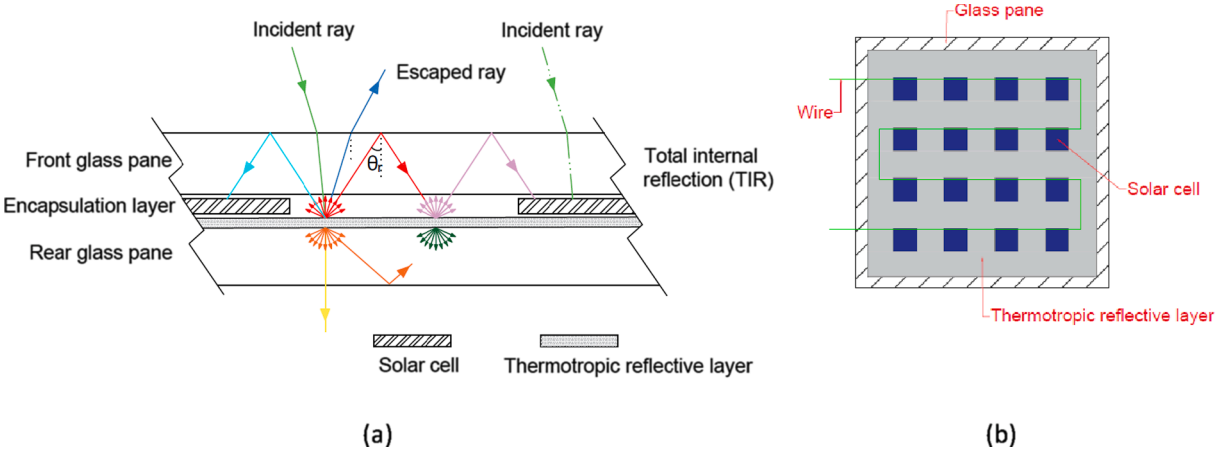

Fig. 1. (a) Cross-sectional and (b) front-view schematic diagrams of the BICPV smart window system.

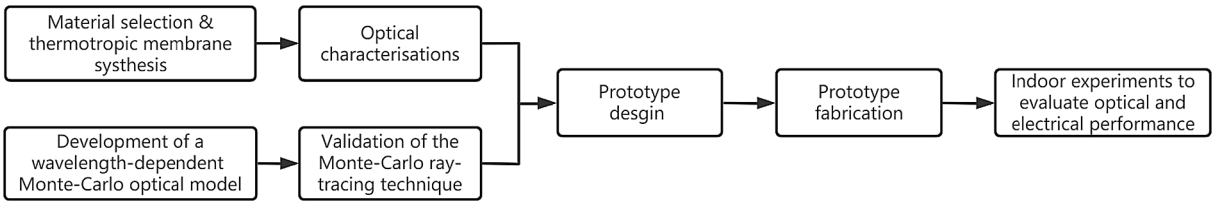

Fig. 2. Flow chart showing the BICPV smart window development process.

in a large area at low costs.

Hydroxypropyl cellulose (HPC) based hydrogels have been proved to be a promising candidate to meet most of the above demands (Allen et al., 2017; Schneider and Seeboth, 2001; Connelly et al., 2016). Moreover, HPC based hydrogels can effectively scatter solar radiation in the wavelength range of 350–1100 nm, which is compatible with the spectral response of c-Si solar cells (Connelly et al., 2017; Connelly et al., 2016). These features make HPC based hydrogels potentially well suited for use in the proposed BICPV smart window system. In this study, the thermotropic reflective layer of the BICPV smart window was synthesised based on HPC and gellan gum (gelling agent) by the following steps:

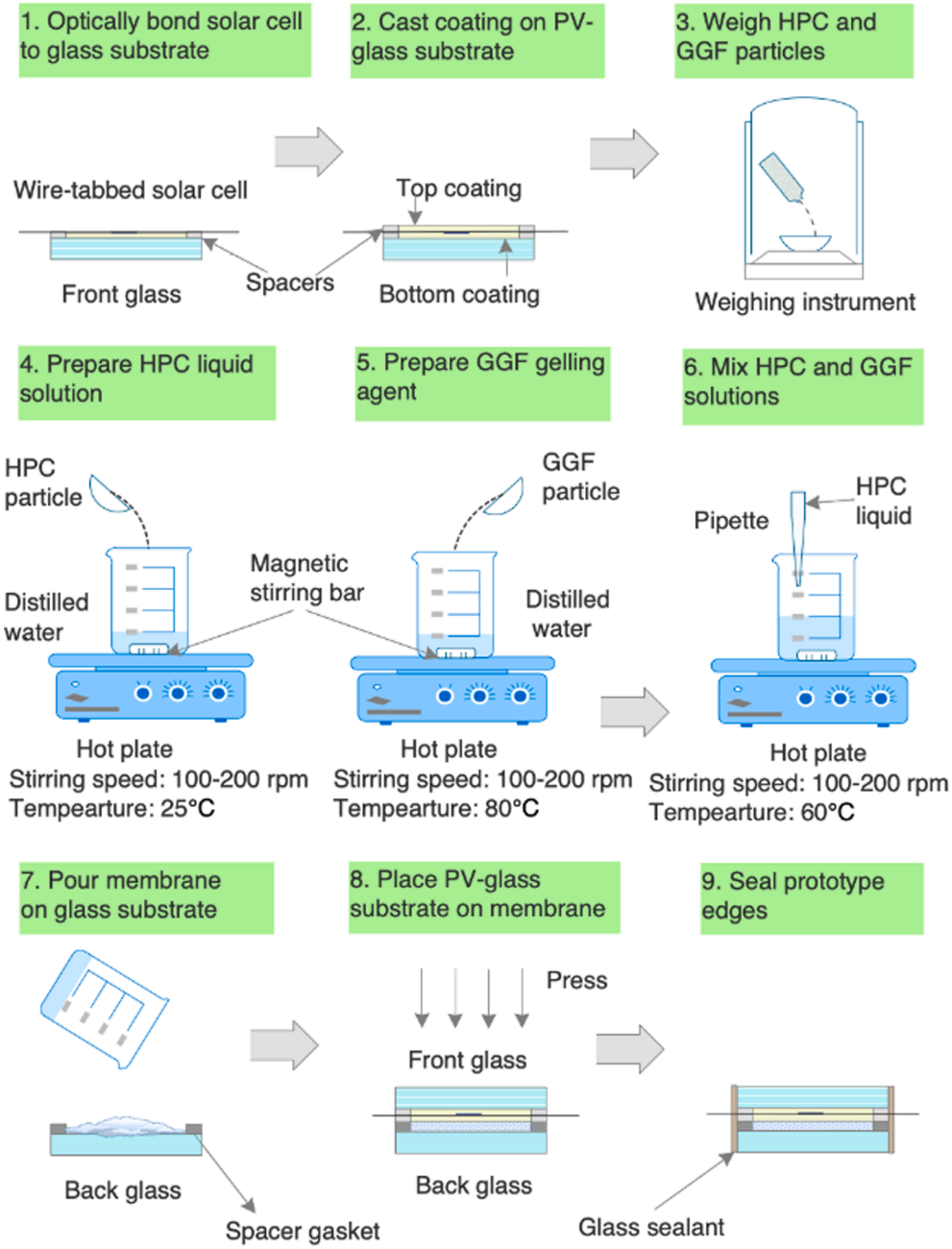

Fig. 3. Prototype fabrication steps.

HPC polymer (weight average molecular weight M_w ~ 80,000 and number average molecular weight M_n ~ 10,000) received as an off-white powder from Sigma Aldrich was magnetically stirred into distilled water at room temperature (25 °C). The stirring was maintained at 100 rpm for several hours until all the HPC had dissolved. A gel matrix was prepared by dissolving Gellan Gum type F (GGF) powder supplied by Special Ingredients in distilled water at 80 °C. A pipette was used to slowly add the HPC aqueous solution into the gel matrix at 60 °C with a stirring speed of 200 rpm. After the addition was completed, the HPC-GGF based aqueous solution was left stirring at 100 rpm with heating off for 10 min. After naturally cooled to the gel state, the HPC-GGF based hydrogel was cast between two GPE Scientific low-iron glass slides spaced by a 1-mm-thick gasket. The HPC-GGF based hydrogel membrane with 1 mm thickness was used for optical characterisations.

3.1.2. Optical characterisations

The spectral transmittance of the HPC-GGF based hydrogel membrane was measured using an Ocean Optics USB2000+UV–VIS-ES spectrometer with an Ocean Optics FOIS-1 integrating sphere. The spectral reflectance was measured using the same spectrometer and an Ocean Optics ISP-REF integrating sphere. The measured spectra had been baseline-corrected (i.e. excluding the spectra of the low-iron glass slides) using the method presented by Connelly et al. (Connelly et al., 2017). A GyroStir-DH hotplate was applied to heat the surface of the laminated glass unit uniformly (within ±1 °C). Meanwhile, the temperature of the HPC-GGF based hydrogel membrane was monitored by an embedded T-type thermocouple that had been waterproofed with epoxy resin adhesive. After the hydrogel membrane was heated to a required temperature, 15 min were allowed for temperature equilibrium before taking the transmittance and reflectance measurements.

3.1.3. Prototype fabrication procedures

A prototype for the designed BICPV smart window system was fabricated following the steps plotted in Fig. 3. Firstly, a Dow-Corning® 1–2577 transparent silicone-based coating with a thickness of 1 mm was cast on a GPE Scientific low-iron glass slide (50 mm × 50 mm × 4 mm), and left to cure at room temperature for 20 min to allow solvents to flash off and blisters to disappear. Next, a Talesun c-Si solar cell (1 cm^2 active area) with its front side facing down was placed at the centre of the coated glass substrate and encapsulated by a second layer of Dow-Corning® 1-2577 coating with 1 mm thickness. The coating was left to solidify at room temperature for 24 h. Subsequently, the synthesised HPC-GGF based hydrogel (following the steps 3–6 detailed in Section 3.1.1) was poured onto a second GPE Scientific low-iron glass slide (50 mm × 50 mm × 4 mm) that had a 1-mm-thick gasket attached to it. Then, the HPC-GGF based hydrogel was covered by the PV-adhered glass

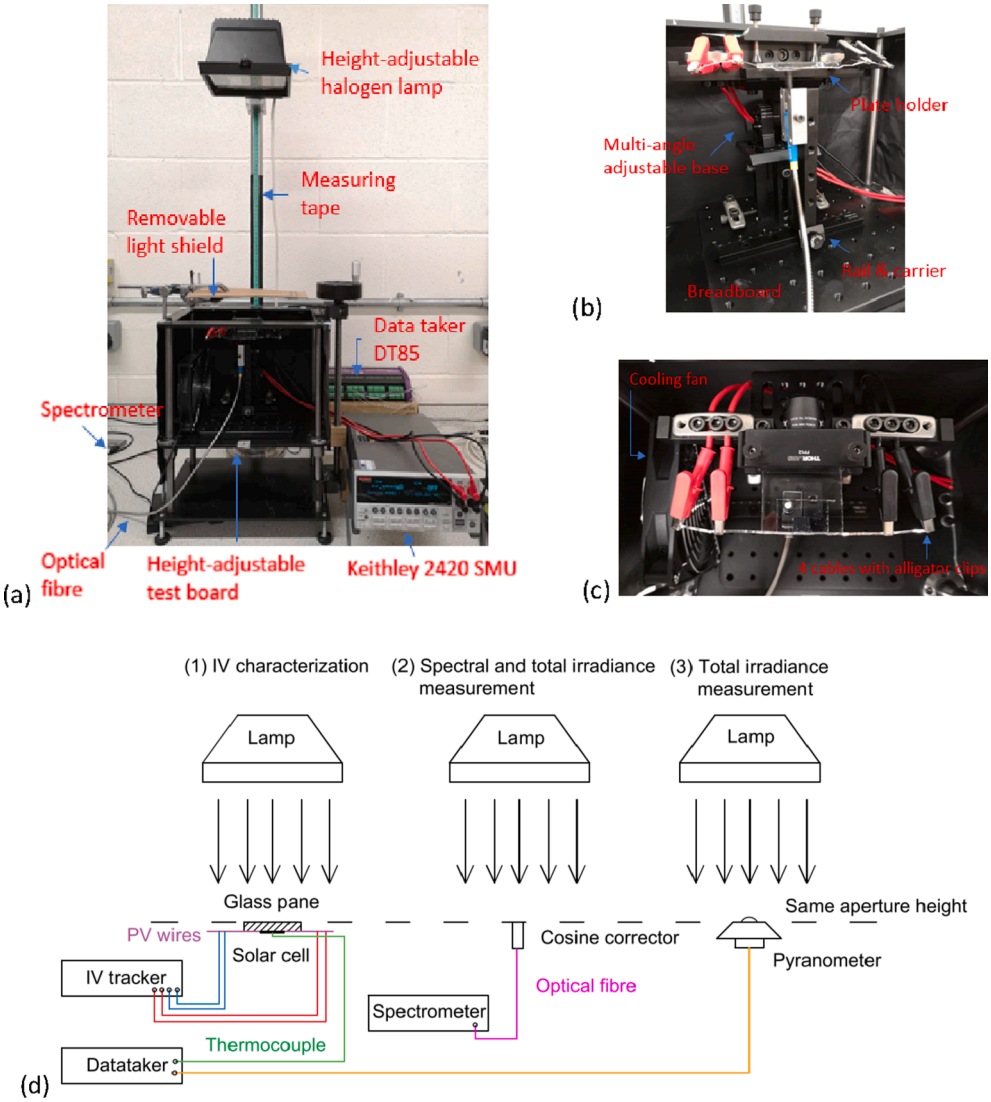

Fig. 4. Photographs and schematic diagram of the indoor experimental setup.

substrate (prepared in step 2) with pressing to get rid of air bubbles. Finally, the laminated glass unit was sealed around the edges using glass sealant and butyl tape to prevent the hydrogel from leaking and drying out, and mounted in a frame made by a 3D printer.

3.1.4. Indoor experimental setup

The BICPV smart window prototype was characterised under indoor conditions using the experimental setup shown in Fig. 4. The sample was mounted on a height-and-angle adjustable holding platform and irradiated by a tungsten halogen lamp. The irradiation level at the sample aperture height was measured with an Ocean Optics optical sampling system consisting of a USB2000+VIS-NIR-ES spectrometer, a CC-3-UV-S cosine corrector and a 200-μm-core-diameter optical fibre. The optical sampling system had been calibrated for absolute spectral irradiance against an Ocean Optics LS-1-CAL halogen light source, and its accuracy had been verified by a Kipp & Zonen CMP11 pyranometer. The irradiation spectrum of the tungsten lamp is presented in Fig. 7. The uniformity of the total irradiance (i.e. the integral value of irradiance spectrum) over the sample aperture area (50 mm × 50 mm) was measured to be within ±5%. The sample was connected to a Keithley 2420 source meter via a 4-wire remote sensing method (Sarmah and Mallick, 2015; Paul et al., 2013; Abu-Bakar et al., 2016) for electrical characterisations. The solar cell temperature and membrane temperature of the sample were detected using a DT85 data logger with T-type thermocouples. The measurements were performed at least in triplicate, and data were expressed as mean ± standard deviation. The specifications of the equipment and sensors are listed in Table 1.

Table 1
Specifications of the experimental devices.

Equipment	Model	Specification and measurement range	Measurement accuracy
Data logger	Datataker DT85	Measuring voltage output from thermocouples; calibrated to ITS-90 standard for thermocouple reading;	0.1% variance for DC voltage (5–40 °C)
Thermocouple	T-type thermocouple	Temperature range of −75 to 250 °C;	±0.5 °C
Spectrometer	Ocean Optic USB2000 + UV–VIS-ES spectrometer	Measuring irradiance, transmittance, reflectance and absorptance; spectral resolution: 0.5 nm;	Signal-to-noise ratio: 250:1
Irradiance detector	Ocean Optics CC-3-UV-S cosine corrector	Collecting light from a 180° Field of view; diffuser diameter: 3900 μm; spectral range: 200 to 2500 nm;	
Optical fibre	Ocean Optics UV–Visible patch cord	Transmitting light; fibre core diameter: 200 μm	
Calibration light source	Ocean Optics LS-1-Cal halogen light source	Calibrating the absolute spectral response of an optical sampling system;	
Pyranometer	Kipp & Zonen CMP11	Spectral range: 285–2800 nm; Field of view: 180°; maximum solar irradiance: 4000 W/m^2	<0.2% non-linearity (100 to 1000 W/m^2)
I-V tracker	Keithley 2420 source meter	Maximum sourcing current: 3A; maximum sourcing voltage: 60 V; minimum resolutions: 1 μV and 100 pA;	0.012% basic measurement accuracy for voltage

3.2. Development and validation of the wavelength dependent Monte-Carlo optical model

Ray-tracing techniques have been widely adopted in the design and performance analysis of solar concentrating systems. The principle is to launch a bundle of rays from a light source and track their trajectories in a solar concentrating system to obtain the irradiance/illuminance at the surface of interest (Nyeinga et al., 2019). For a mirror or lens-based solar concentrator, the incident ray paths are altered by specular reflection or refraction at the geometrical surfaces (Su et al., 2012; Sarmah et al., 2011). For a diffuse type solar concentrator, when light encounters a diffuse surface/body, it is scattered into a wide range of directions. This phenomenon can be modelled using a stochastic sampling method, named Monte-Carlo ray-tracing technique. In principle, the continuous light scattering distribution is approximated by a set of random rays with possible directions (Meinardi et al., 2017) (see Fig. 5). The directions of scattered rays are randomly selected according to a prescribed probability distribution function (Montes and Ureña, 2012; Jensen et al., 2003). Due to the stochastic nature of the Monte-Carlo ray-tracing process, a large quantity of rays is required to be traced in order to achieve a good approximation (Wu et al., 2016; Burgers et al., 2005).

3.2.1. Optical model description

A Monte-Carlo ray-tracing simulation approach coupled with measured material properties was developed to predict the radiation characteristics of the BICPV smart window system. A Monte-Carlo ray-tracing model was set up in the software TracePro, involving four steps: (1) constructing the geometry of the system; (2) applying measured spectral properties to the geometrical components; (3) defining rays emitted from a light source; (4) propagating rays through the system and calculating the flux on the absorber surfaces (solar cells).

In designing the prototype system, a 3D model geometry was created with a single solar cell and a four-layer stacked structure: front glass cover, optical coating layer, thermotropic membrane layer and back glass cover, similar as seen in Fig. 1. The geometric design parameters, such as glass cover thickness and aperture area, were determined through a parametric analysis (detailed in Section 5.1.2). The optical model assumed the thermotropic membrane layer as a Lambertian-type diffused reflector, i.e., a surface reflecting light equally in all view directions (i.e. no angular dependence) (Li et al., 2014; Schaepman-Strub et al., 2006; Simonot, 2009). The spectral reflectance and transmittance at different temperatures of the thermotropic membrane layer were measured (see Fig. 12) and used as the Lambertian surface properties. The glass covers and optical coating were defined with the wavelength-dependent optical constants, including refractive index (n) and absorption coefficient (α), calculated by Eqs. (2)–(7) (Rubin et al., 1998) and shown in Fig. 6. For simplicity, the front side of the solar cell was assumed as a perfect absorber of light (with 100% optical absorptance), while its back side was assumed as a perfect Lambertian surface (with 100% diffuse reflectance). To match the laboratory conditions as closely as possible, the spectral irradiance of the light source was equal to the result measured for the applied tungsten halogen lamp (see Fig. 7). The

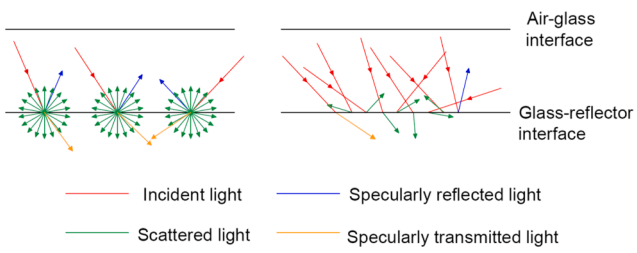

Fig. 5. Schematic diagrams of light scattering at a surface in reality (left diagram) and modelled by a Monte-Carlo ray-tracing technique (right diagram). Note: scattering is a 3D phenomenon, but here shown in 2D.

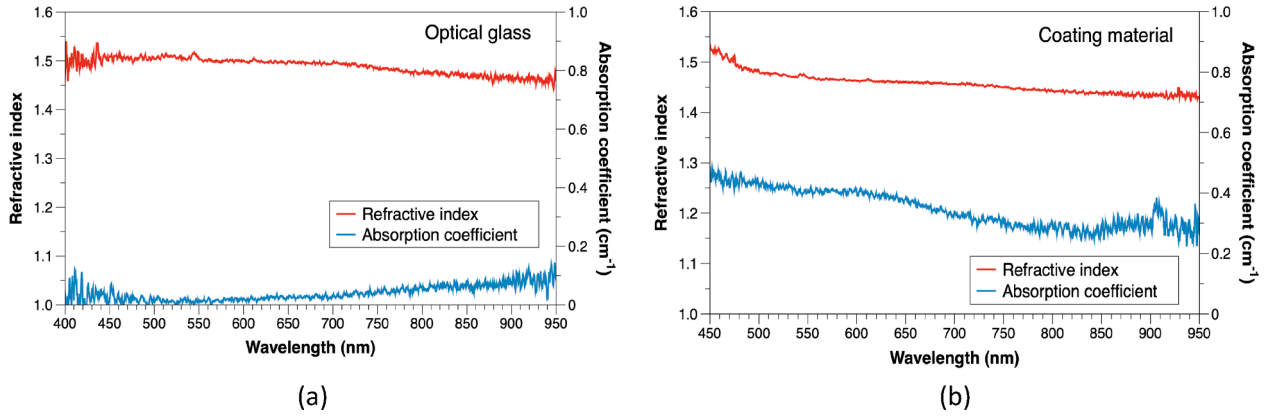

Fig. 6. Calculated spectral absorption coefficient and refractive index for (a) the GPE Scientific low-iron glass slide and (b) the Dow-Corning® 1-2577 coating layer.

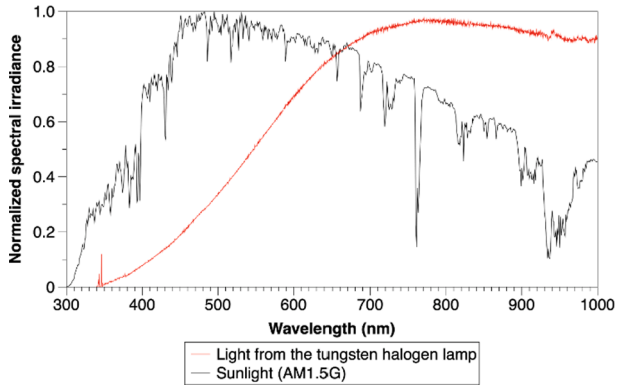

Fig. 7. Normalised irradiation spectrum of the tungsten halogen lamp compared with the normalised standard AM1.5G solar spectrum.

number of the rays, which were emitted from the light source and perpendicularly applied to the aperture of the front glass cover of the prototype system, was set to 1,000,000 according to a ray-independence study.

In the process of tracing a ray through the system, the outcome of events (transmission, reflection, scattering and absorption) was determined by the Monte-Carlo method (Nitz et al., 1998; Leow et al., 2013; Lambda Research Corporation, 2020). Specifically, each time the ray intersects a surface, the surface properties (specular/diffuse transmittance, specular/diffuse reflectance and absorptance) are used as probabilities and compared to a randomly generated number (between 0 and 1); for example, for a non-absorbing surface with 30% reflectance and 70% transmittance, if the number is between 0 and 0.3, the ray is reflected, otherwise the ray is transmitted. The process continues until the ray is lost from the system, absorbed by the solar cell or attenuated with its energy flux below the predefined threshold 5% (i.e. fraction value of starting energy flux).

$$n = \frac{1+\sqrt{r_s}}{1-\sqrt{r_s}} \tag{2}$$

$$\alpha = \frac{4\pi k}{\lambda} \tag{3}$$

$$r_s = \frac{\beta - \sqrt{\beta^2 - 4(2-R_s)R_s}}{2(2-R_s)} \tag{4}$$

$$\beta = T_s^2 - R_s^2 + 2R_s + 1 \tag{5}$$

$$k = -\frac{\lambda}{4\pi d}\ln\tau_S \tag{6}$$

$$\tau_S = \frac{R_s - r_s}{r_s T_S} \tag{7}$$

where n is the refractive index of the substrate, α is the absorption coefficient of the substrate, r_s is the reflectance at the air-substrate interface, τ_s is the internal transmission of the substrate, R_s and T_s are the directional-hemispherical reflectance and transmittance of the substrate obtained from spectroscopy measurements, k is the extinction coefficient of the substrate, d is the substrate thickness, λ is wavelength.

3.2.2. *Validation of the Monte-Carlo ray-tracing model*

Prior to the design of the prototype system, a preliminary verification of the proposed Monte-Carlo ray-tracing technique by indoor experimental tests was carried out. The validation samples were manufactured with a GPE Scientific low-iron glass slide (50 mm × 50 mm × 4 mm), a Talesun c-Si solar cell and different types of static diffuse reflective film, as shown in Fig. 8. The c-Si solar cell has dimensions of 1 cm × 1.2 cm (1 cm^2 active area) and the electrical properties: 35 mA short-circuit current, 611 mV open-circuit voltage, 0.768 fill factor and 16.5% power conversion efficiency at standard test conditions (100 mW/cm^2 illumination, AM1.5 solar spectrum and 25 °C cell temperature). The solar cell was tabbed with Ulbrich tin-coated copper PV wires (1.8 mm wide and 0.1 mm thick) using a low-melting-point tin/lead solder. The wire-tabbed solar cell and the static diffuse reflective film were optically bonded to the low-iron glass slide. The optical bonding was achieved using a Dow-Corning® 1–2577 transparent silicone-based coating, whose thickness on the glass substrate was uniformly controlled at 0.5 mm through the tape casting technique (also called doctor-blade method) (Ahmadi et al., 2014; Chen and Ting, 2013). Before testing, it is important to ensure that the active area of the solar cell is in complete contact with the coated glass substrate with no solder bump and air gap in-between; otherwise, these would affect the experiment validation due to a reduced amount of light collected by the solar cell (Zhang et al., 2015).

The static diffuse reflective films are commercially available frosted films, named plain frosted film (Purlfrost®), white frosted film (Purlfrost Ltd®), milky frosted film (d-c-fix®) and opal frosted film (Purlfrost®). These frosted films are a type of solar control film for windows to scatter sunlight in the visible range and reduce glare. Their spectral transmittance and reflectance films were measured using the same spectroscopy method and optical devices as for the thermotropic membrane.

It can be seen from Fig. 9(a) that the plain frosted film has the highest transmittance in the wavelength range from 400 to 950 nm, followed by the white frosted, milky frosted and opal frosted films; for example, the values at the 600 nm wavelength are 92.5% (plain frosted film), 75.2%

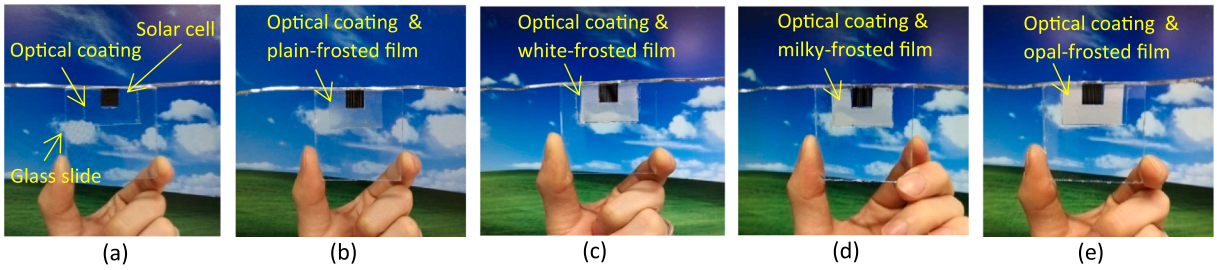

Fig. 8. PV modules with (a) no film, (b) a plain-frosted film, (c) a white-frosted film, (d) a milky-frosted film and (e) an opal-frosted film. The ratio between the solar cell area and the frosted film area is 1:5.

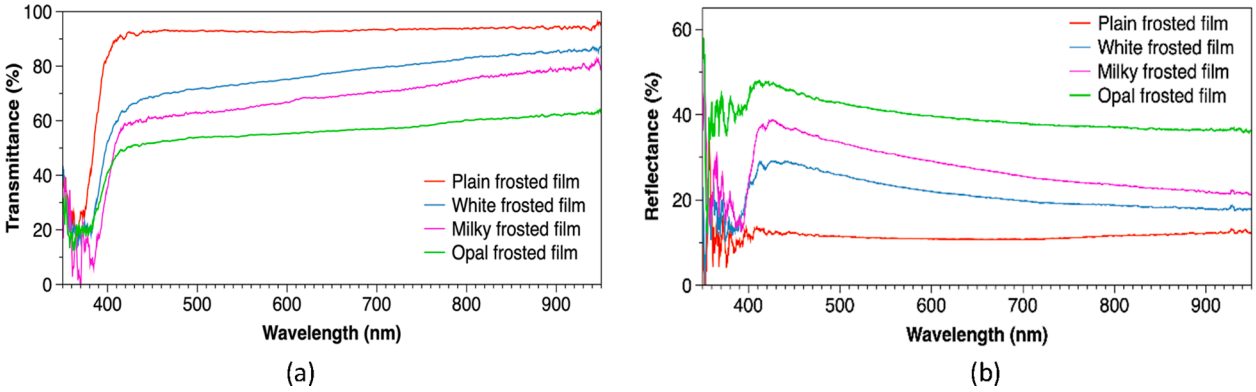

Fig. 9. (a) Spectral transmittance and (b) spectral reflectance of the frosted films from 350 to 950 nm.

(white frosted film), 66.8% (milky frosted film) and 55.3% (opal frosted film), respectively. Conversely, the opal frosted film has the highest reflectance over the 400–950 nm spectrum, followed by the milky frosted, white frosted and plain frosted films, as shown in Fig. 9(b); for example, the values at 600 nm are 40.4% (opal frosted film), 30.2% (milky frosted film), 22.9% (white frosted film) and 10.1% (plain frosted film), respectively. The purpose of using these different static diffuse reflective films is to acquire preliminary observations on the effect of the dynamic reflectance of the developed thermotropic membrane on PV electricity generation.

The electrical characteristics of the fabricated samples including the reference PV module (with no film) were measured using the setup shown in Fig. 4. From Fig. 10 and also Fig. 11(a), it can be seen that the sample based on the opal frosted film has both the highest short-circuit current (17.6 mA) and maximum power output (8.5 mW), followed by the samples based on the milky frosted film (17.0 mA and 8.3 mW), the white frosted film (16.8 mA and 8.1 mW), the plain frosted film (16.1 mA and 7.8 mW) and with no film (15.1 mA and 7.3 mW). The sequence is the same as that found for the reflectance measurement. The result suggests that using a diffuse reflective film with higher reflectance for application in PV glazing can contribute to improved electricity generation.

The fabricated samples were optically modelled using the proposed Monte-Carlo ray-tracing technique. The model settings are the same as those described in Section 3.2.1, except using the measured spectral properties for the static diffuse reflective films as input. The simulated irradiance on the solar cell surface for the samples is shown in Fig. 11(b). The irradiance is increased from 423.1 to 447.7 W/m^2 when the reference PV module is integrated with the plain frosted film, and further to 489.5 W/m^2 when integrated with the opal frosted film with higher reflectance. The result indicates that increasing the reflectance of the diffuse reflective film yields a more substantial solar concentration effect.

As known from the literature (Sharaf and Orhan, 2015; Xuan et al., 2019), the short-circuit current produced by a crystalline-silicon solar cell can be taken as directly proportional to the solar irradiance on it,

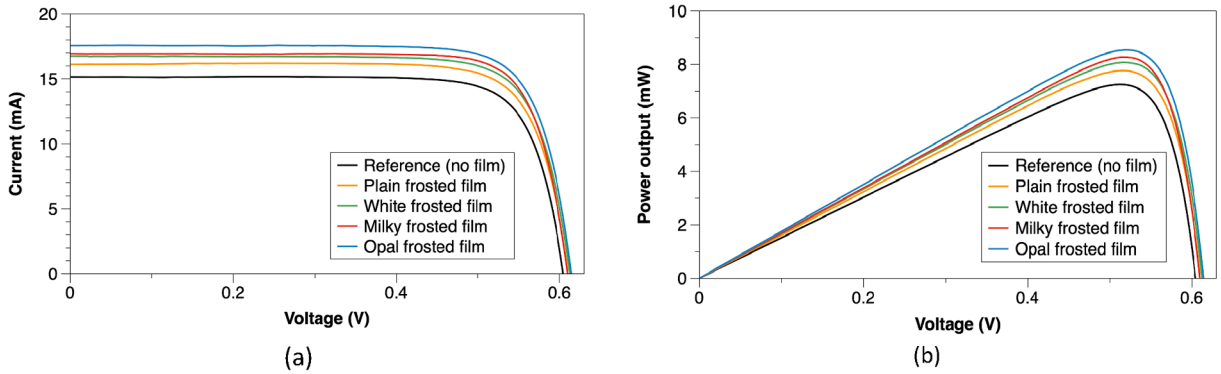

Fig. 10. (a) Current-voltage (I-V) characteristics and (b) power-voltage (P-V) characteristics of the PV modules at a cell temperature of 25 °C and under an incident radiation level of 460 W/m^2.

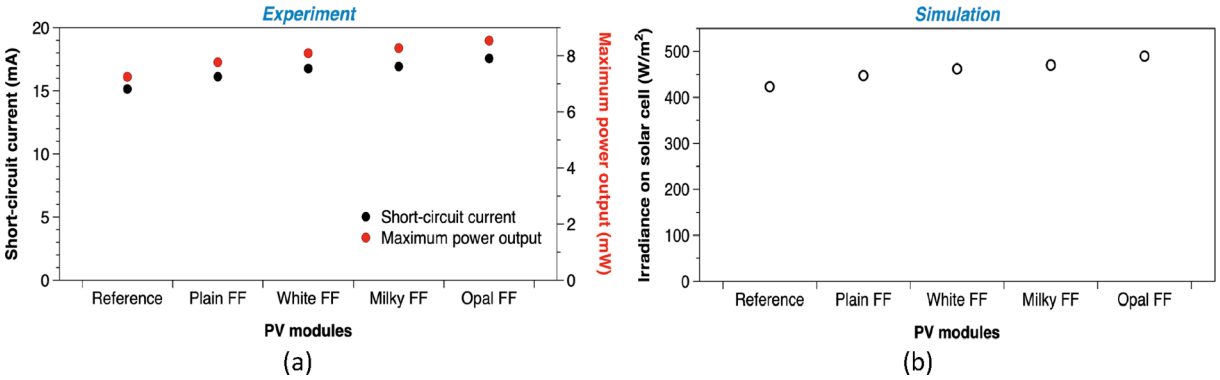

Fig. 11. (a) Measured electrical properties and (b) simulated irradiance on the solar cell for the PV modules based on different frosted-films (FF) and the reference PV module with no film.

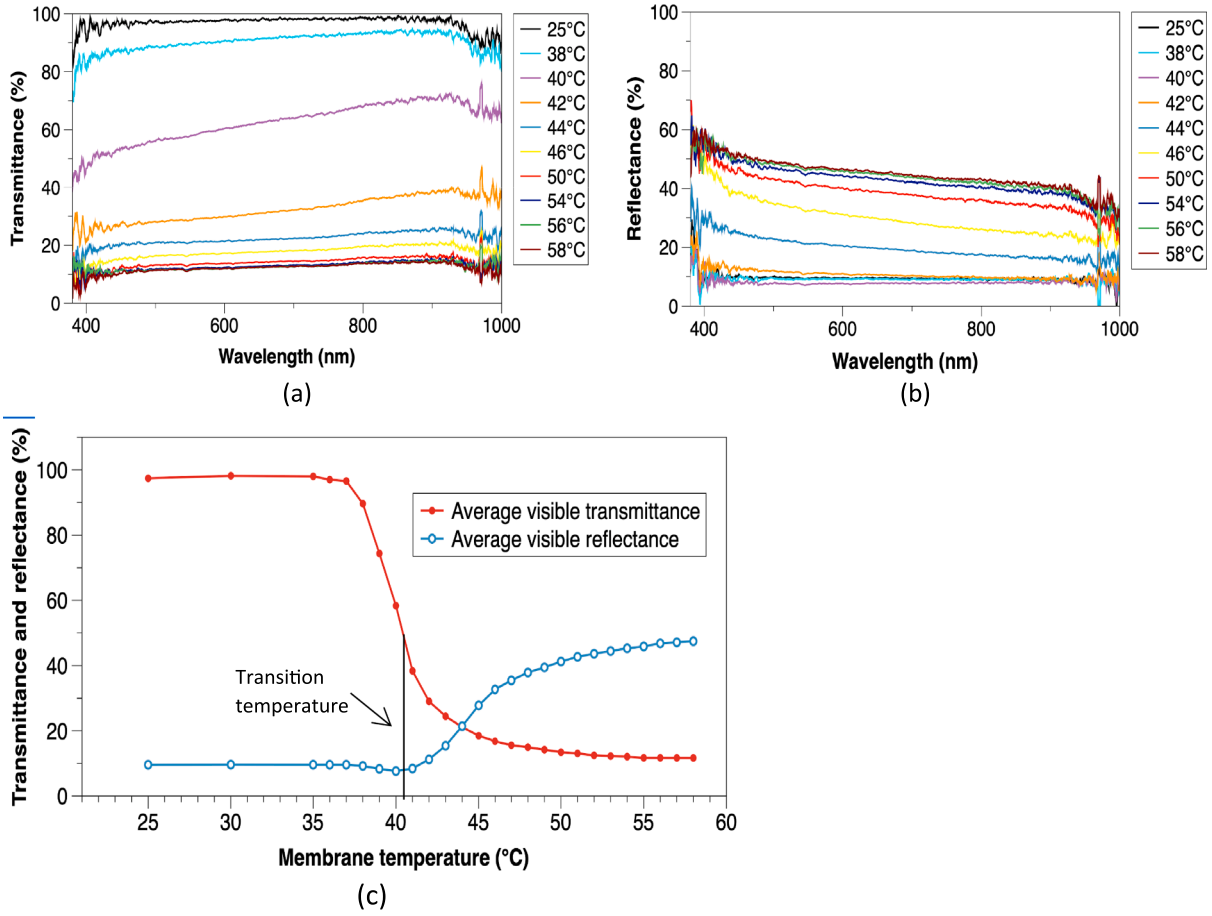

Fig. 12. (a) Spectral transmittance, (b) spectral reflectance and (c) average visible light transmittance and reflectance of the 6 wt% HPC and 1.5 wt% GGF based hydrogel membrane with 1 mm thickness under various membrane temperature conditions.

which allows using irradiance or optical concentration ratio as an indication of short-circuit current. Therefore, the short-circuit current of a concentrating PV module could be expressed by Eq. (8) (Baig et al., 2020; Li et al., 2014; Nilsson, 2005) with respect to a reference case. This equation together with the experimental result was applied for validating the developed optical models. As compared in Table 2, the deviation between the ratio of short-circuit-currents (from the experiment) and the ratio of irradiances (from the optical simulation) is less than 1.5% for all the static diffuse reflective film cases. Therefore, the proposed Monte-Carlo ray-tracing technique can be considered as a reliable approach for the design and optical analysis of diffuse-type solar concentrators.

$$\frac{I_{sc}}{I_{sc,ref}} = \frac{G}{G_{ref}} \tag{8}$$

where I_{sc} is the short-circuit current of the concentrating PV module, $I_{sc,ref}$ is the short-circuit current of the reference PV module with no concentrator, G is the irradiance on the PV cell under solar concentration, G_{ref} is the irradiance on the reference PV cell.

Table 2
Comparison between the simulated and measured results for the tested PV modules.

	Reference	Plain FF	White FF	Milky FF	Opal FF
Reflectance at 600 nm		10.1%	22.9%	30.2%	40.4%
Measured short-circuit current (mA)	15.14	16.12	16.76	16.95	17.56
Current ratio ($I_{sc}/I_{sc,ref}$)	–	1.065	1.107	1.120	1.160
Simulated irradiance (W/m^2)	423.1	447.7	462.5	470.4	489.5
Irradiance ratio (G/G_{ref})	–	1.058	1.093	1.112	1.157
Difference between the ratios		0.62%	1.25%	0.68%	0.25%

4. Results and discussion

4.1. BICPV smart window prototype design and development

4.1.1. Thermotropic membrane properties

Fig. 12 shows the spectral transmittance and reflectance of a 1-mm-thick thermotropic hydrogel membrane synthesised of 6 wt% HPC and 1.5 wt% GGF. The average light transmittance (T_{vis}) and reflectance (R_{vis}) in the visible region (380–780 nm) of the hydrogel membrane were calculated by Eqs. (9) and (10) (BS EN 410:2011, 2011), respectively. From Fig. 12(a), it can be seen that the spectral transmittance reduces from over 90% to about 10% with an increase in membrane temperature from 25 to 58 °C. A transition temperature of 40.5 °C is recorded (see Fig. 12(c)). Here, the transition temperature is quoted as the temperature at which the average visible light transmittance equals to 50% of the transmittance at 25 °C. On the other hand, the spectral reflectance increases from approximately 10% to over 40% when the temperature increases from 25 to 58 °C, as shown in Fig. 12(b). The sharp changes in transmittance and reflectance are caused by phase separation in the hydrogel membrane, where HPC polymer chains aggregate and free water quenches out of the polymer network, owing to the weakening of hydrogen bonding between HPC polymer chains and surrounding water molecules by heating (Allen et al., 2017; Connelly et al., 2017). The formation of local differences in refractive index between the HPC aggregation and water matrix induces light scattering in the hydrogel membrane (Resch and Wallner, 2009). As can be seen from Fig. 12(a–c), the further temperature elevation from 54 to 58 °C leads to insignificant changes in transmittance and reflectance, indicating the near completion of phase separation. At 58 °C, the average visible light transmittance and reflectance are 11.7% and 47.1%, respectively.

$$T_{vis} = \frac{\sum_{380nm}^{780nm} D_\tau T(\lambda) V(\lambda) \Delta\lambda}{\sum_{380nm}^{780nm} D_\tau V(\lambda) \Delta\lambda} \quad (9)$$

$$R_{vis} = \frac{\sum_{380nm}^{780nm} D_\tau R(\lambda) V(\lambda) \Delta\lambda}{\sum_{380nm}^{780nm} D_\tau V(\lambda) \Delta\lambda} \quad (10)$$

where $T(\lambda)$ is the measured spectral transmittance, $R(\lambda)$ is the measured spectral reflectance, $\Delta\lambda$ is the interval between wavelengths, $V(\lambda)$ is the spectral luminous efficiency for photopic vision defining the standard observer for photometry, and D_τ is the relative spectral distribution of illuminant D65.

4.1.2. Predicted optical performance

A prototype for the BICPV smart window system was designed with the aid of the validated Monte-Carlo ray-tracing model. Fig. 13 shows the main components comprising the prototype. The thermotropic reflective layer was for simplicity modelled as a Lambertian surface between the back glass cover and the optical coating layer. The dynamic reflectance of the Lambertian surface was assumed to be in the range of 10–47%, according to the optical measurement (displayed in Fig. 12).

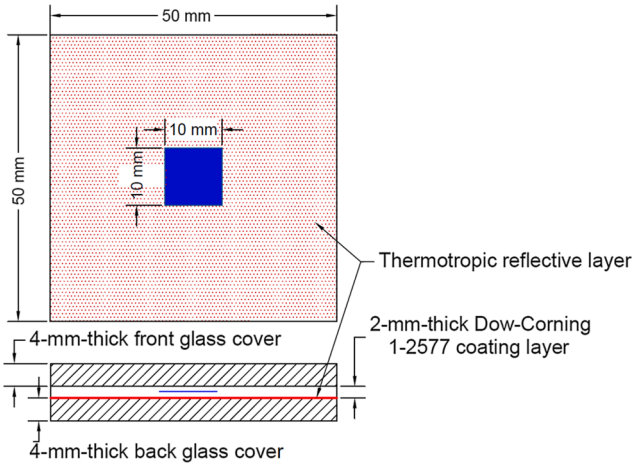

Fig. 13. Model geometry of the BICPV smart window prototype.

Optical simulations were conducted for a series of the designed prototypes with respect to different glazing aperture areas (between 20 mm × 20 mm and 80 mm × 80 mm) and different glazing cover thicknesses (between 1 and 8 mm). The optical concentration ratio, which is denoted as the ratio of the irradiance on the solar cell surface to the irradiance on the front glazing aperture, was calculated for the different design scenarios.

As can be seen from Fig. 14(a), the optical concentration ratio of the designed prototypes is strongly dependent on the reflectance of the thermotropic layer. Take the prototype with the front glass cover dimensions of 50 mm × 50 mm × 4 mm as an example: the optical concentration ratio increases from 0.96 to 1.15 when the reflectance increases from 10% to 47%. Significant improvements in optical concentration ratio are observed by increasing the glazing aperture area until it exceeds 70 mm × 70 mm. This indicates that further extensions of the glazing aperture area could not contribute to more photons being collected by the solar cell, due to the losses of photons caused by multiple scattering, absorption and escaping. In terms of the front glass cover thickness, the optical concentration ratio is maximum at the thickness of 3 or 4 mm, as shown in Fig. 14(b). This may be because a higher thickness results in longer paths for the photons travelling in the front glass cover before reaching the solar cell and thus higher optical absorption; however, reducing the thickness may cause more scattered photons escaping from the front glass cover, due to an increased number of light pass between the boundaries of the front glass cover, i.e., a higher possibility for light entering the glass-air interface at angles less than the critical angle.

Considering the balance between the predicted optical concentration ratio and the uniformity of the indoor lamp irradiation over the sample aperture area (>5% errors when the sample aperture area is greater than 50 mm × 50 mm), the dimensions of the front glazing cover were selected as 50 mm × 50 mm × 4 mm for the prototype fabrication. Optical simulations have also been conducted for different thicknesses of the back glass cover, however, which show only a minor effect on the optical concentration ratio.

4.2. Electrical and solar control performance

A prototype of the optimised design (Fig. 13) for the BICPV smart window system was fabricated and evaluated by an indoor experiment. The electrical and optical performance of the prototype along with the membrane temperature and solar cell temperature were measured simultaneously. Fig. 15 shows the transition process of the prototype from a clear state to a light-scattering state with an increase in membrane temperature. The light transmitted through the prototype was detected by the cosine-corrected irradiance probe held against the

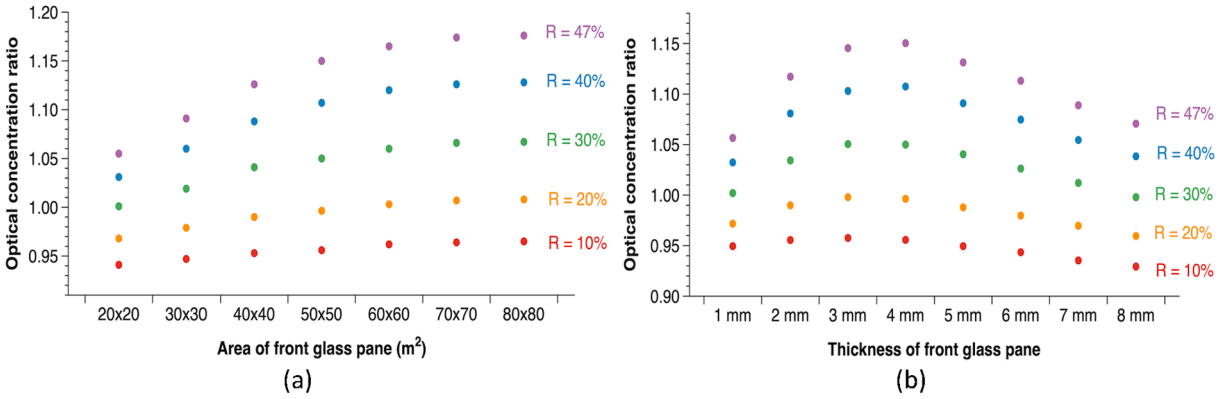

Fig. 14. Optical concentration ratio of the BICPV smart window (a) for different aperture areas of the front glazing with the same thickness 4 mm and (b) for different thicknesses of the front glazing with the same aperture area 50 mm × 50 mm; the reflectance (R) of the thermotropic layer is assumed to vary between 10% and 47%.

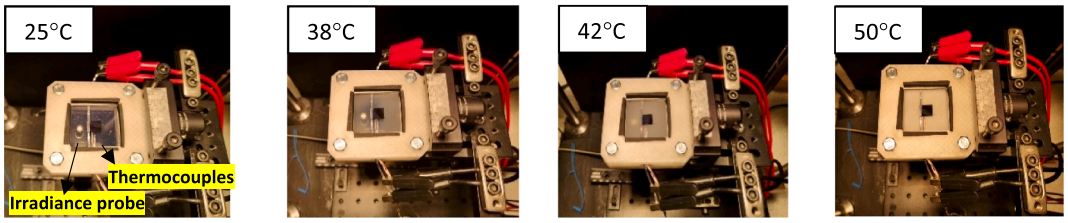

Fig. 15. Images illustrating the state transition of the BICPV smart window prototype with the membrane temperature increasing.

prototype's backside. The solar cell temperature and membrane temperature were monitored by the T-type thermocouples, which had been calibrated and wrapped with aluminium foil to avoid any light exposure.

4.2.1. Effect of membrane temperature

Fig. 16 shows the electrical characteristics of the BICPV smart window prototype with a 6 wt% HPC and 1.5 wt% GGF based hydrogel membrane under varying membrane temperatures. No significant differences in short-circuit current (i.e. current at the voltage of 0 V) and maximum power output (i.e. the peak point of a P-V curve) are observed between 28 °C and 40 °C. Further increasing the membrane temperature to above 40 °C yields significant increases in short-circuit current and maximum power output. This is because the HPC-GGF based hydrogel membrane above 40.5 °C transitions from a transparent state to a light-scattering state, resulting in more light being collected by the solar cell. As can be seen from Fig. 17(a), the short-circuit current produced by the BICPV smart window prototype increases from 26.9 to 31.9 mA with the membrane temperature increasing from 40 to 50 °C; meanwhile, the maximum power output increases from 12.1 to 14.1 mW. In contrast, the counterpart PV window system, which has a similar structure but without the hydrogel membrane, shows a continuous decline in maximum power output and a slight increase in short-circuit current with the increasing solar cell temperature (see Fig. 17(b)). The maximum power output and short-circuit current of the counterpart PV window system are 12.7% and 17.4% lower than those of the BICPV smart window prototype, respectively, when the solar cell temperature reaches 55 °C.

The electrical characteristics of the BICPV smart window prototype and its counterpart system were also compared under different conditions of incident light intensity and angle. Fig. 18(a) shows the I-V characteristics at a solar cell temperature of 50 °C under the three irradiation levels: 550, 600 and 700 W/m^2. The short-circuit current of the BICPV smart window prototype is observed to increase from 31.9 to 41.0 mA when the irradiation level is elevated from 550 to 700 W/m^2.

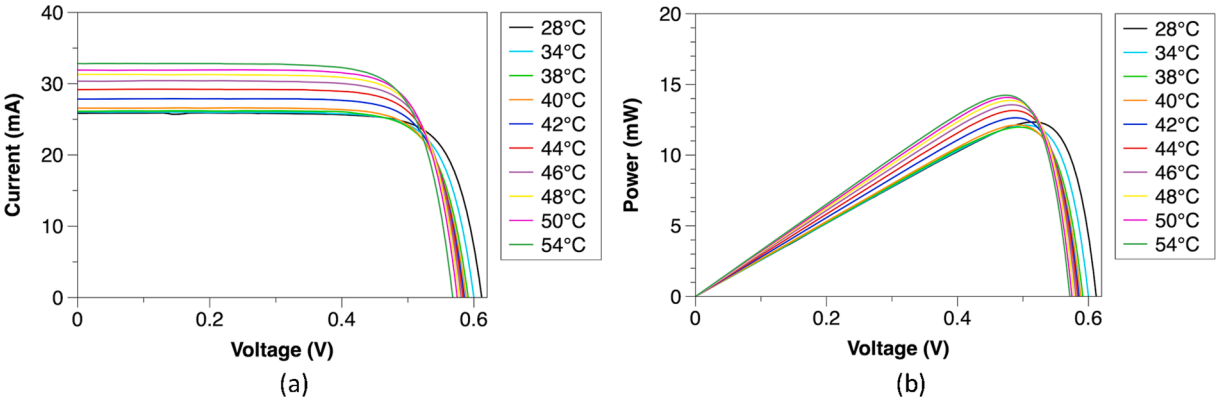

Fig. 16. (a) I-V and (b) P-V characteristics of the 6 wt% HPC and 1.5 wt% GGF based BICPV smart window prototype under different membrane temperatures and an irradiation level of 550 W/m^2.

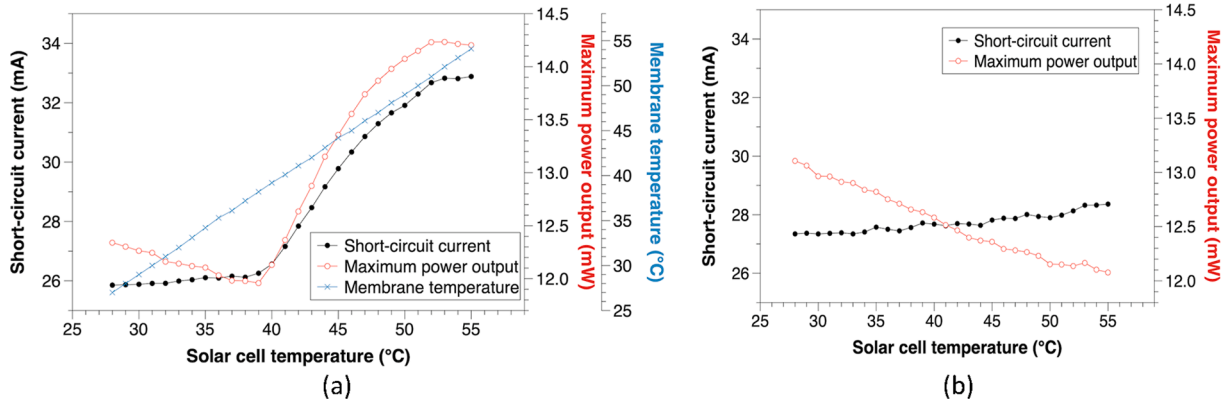

Fig. 17. Short-circuit current and maximum power output of (a) the BICPV smart window prototype and (b) its counterpart with no membrane, as a function of solar cell temperature.

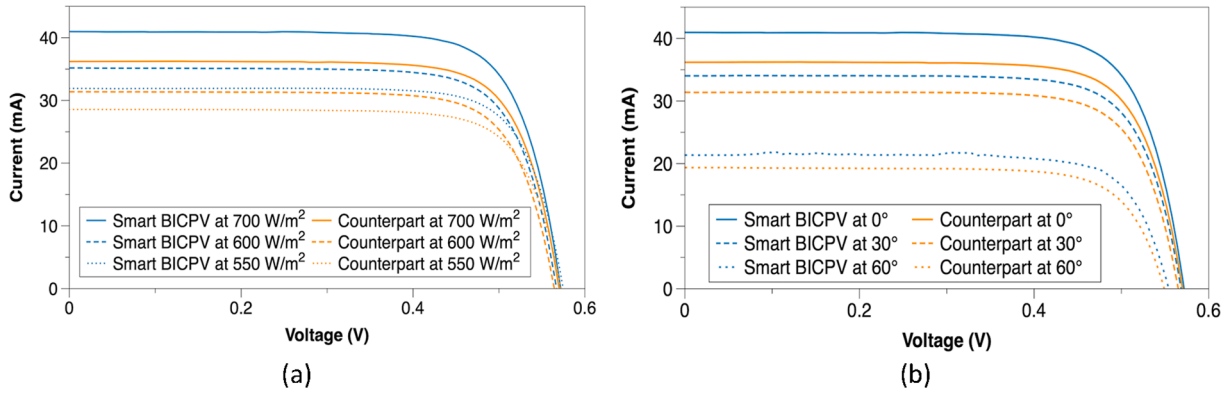

Fig. 18. I-V characteristics of the BICPV smart window prototype and its counterpart system (a) under the irradiation levels of 550, 600 and 700 W/m^2 at the incident light angle of 0°, and (b) at the incident light angles of 0°, 30° and 60° under the irradiation level of 700 W/m^2.

Under the same irradiation levels, the BICPV smart window prototype has both higher short-circuit currents and power outputs (i.e. current times voltage) compared with its counterpart system. From Fig. 18(b), it can be seen that the short-circuit current of the BICPV smart window prototype under 700 W/m^2 irradiation decreases from 41.0 to 21.3 mA when the incident light angle is increased from 0° (normal to the plane) to 60°. At the same incident light angles, the BICPV smart window prototype offers better electrical performance than its counterpart system.

4.2.2. *Effect of HPC concentration*

The effect of HPC concentration on the electrical and optical performance of the BICPV smart window prototype has been investigated. Three hydrogel membranes consisting of 1.5 wt% GGF and different HPC concentrations (2, 4 and 6 wt%) were prepared for the comparative analysis. As can be seen from Fig. 19(a), the maximum power outputs of

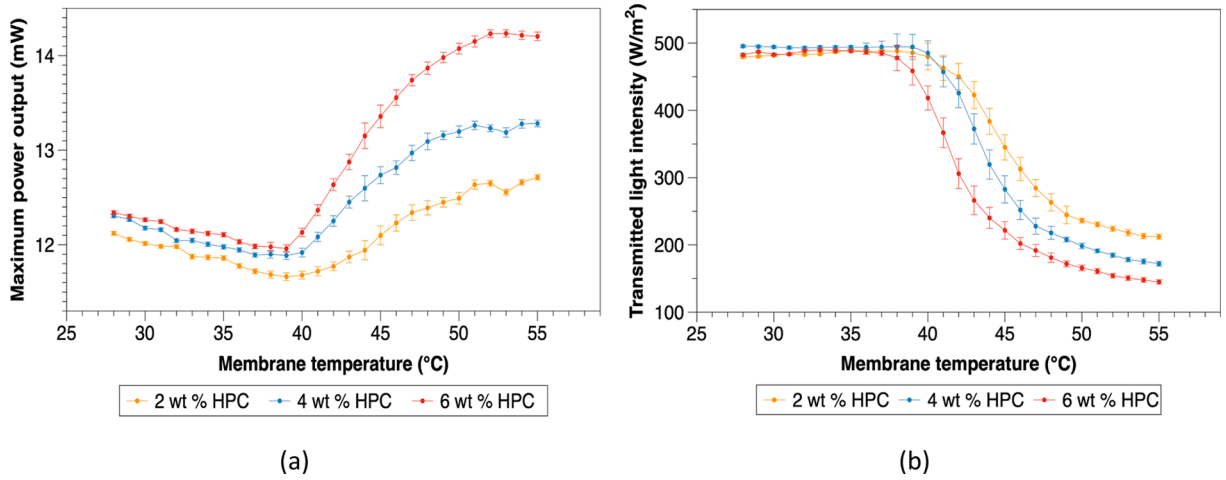

Fig. 19. (a) Maximum power output and (b) transmitted radiant intensity of the 2, 4 and 6 wt% HPC based BICPV smart window prototypes as a function of membrane temperature under an irradiation level of 550 W/m^2. Error bars represent one standard deviation.

the three BICPV smart window prototypes show decreasing trends when the membrane temperature increases from 28 to 39 °C. This is because of the fact that under constant irradiation, the power conversion efficiency of c-Si solar cells decreases with an increase in operating temperature (Brano et al., 2010). The maximum power outputs of the three prototypes start to increase once the membrane temperature exceeds 40 °C, due to the occurrence of phase separation. The 6 wt% HPC based prototype shows a 17.1% increase in the mean value of maximum power output with the membrane temperature increasing from 40 to 54 °C, followed by the prototypes based on 4 wt% HPC (11.5%) and 2 wt% HPC (8.9%). On the other hand, the mean values of the intensity of the light transmitted through the prototypes based on 6 wt%, 4 wt% and 2 wt% HPC reduce by 70.9%, 66.5% and 57.3%, respectively, when the membrane temperature increases from 28 to 54 °C, as shown in Fig. 19 (b). The outcomes may be attributed to higher reflectance and lower transmittance of the hydrogel membranes with greater HPC concentrations (Connelly et al., 2017; Connelly et al., 2016), because of more HPC aggregates formed in the water matrix during phase separation.

The above experimental results demonstrate that the BICPV smart window system has the potential to provide lower solar heat gains and higher electricity generation when subjected to higher membrane temperatures, which could protect the building interior from overheating in summer and improve the building energy efficiency. The optical analysis reveals that the effectiveness of solar concentration via total internal reflection is related to the thermotropic membrane reflectance as well as the optical losses due to escaping of light from the system. The thermotropic membrane reflectance could potentially be further enhanced by increasing the HPC concentration, HPC particle size or membrane thickness. The optical losses may be reduced by applying low-iron glass covers with a higher refractive index. The optimisation, however, should also take into account the reduction in daylight transmission and the impacts on occupant comfort and building energy consumption.

5. Conclusions

A Building Integrated Concentrating Photovoltaic (BICPV) smart window with a dual function of electricity generation and adaptive solar radiation control has been introduced in this project. A validated Monte-Carlo ray-tracing technique has been applied for the system design and performance prediction. A thermotropic hydrogel membrane comprised of 6 wt% HPC and 1.5 wt% GGF has been selected for the BICPV smart window system due to its relative higher reflectance than the other type of wt% HPC and GGF when above transition temperature and also meet most of the window requirements. From the optical prediction, it can be seen that the prototype with a 50 mm × 50 mm × 4 mm front glass cover and a 10 mm × 10 mm solar cell exhibits better electrical performance than the other designs of similar aperture size but with different thickness. A prototype with this suggested design has been subsequently fabricated and characterised experimentally. Some key findings from the BICPV smart window characterisations are presented below:

1 The maximum power output of the BICPV smart window system decreased with an increase in membrane temperature until reaching the HPC thermotropic membrane transition temperature of 40.5 °C; it increased significantly thereafter.
2 The BICPV smart window system offered a higher short-circuit current and a higher maximum power output by up to 12.7% and 17.4%, respectively, compared to its counterpart system with no HPC thermotropic membrane applied.
3 An approximately 70% reduction in light transmittance for the BICPV smart window system was observed when the membrane temperature increased from 28 to 54 °C.
4 Using a higher HPC concentration could potentially enhance both solar transmittance modulation and electricity generation of the system.

Overall, this project reveals that the proposed BICPV smart window system has the potential to enhance the on-site electricity generation and reduce the risks of overheating and glare in buildings when compared to traditional non-concentrating PV windows. Future work will need to be carried out to adjust the transition temperature and optimise the light-scattering properties of the thermotropic hydrogel membrane to make it more suitable for building applications. Building energy simulation will need be performed to evaluate the daylight performance and energy-saving potential of the BICPV smart window system.

Declaration of Competing Interest

The authors declare that they have no known competing financial interests or personal relationships that could have appeared to influence the work reported in this paper.

Acknowledgement

This work was supported by the Faculty of Engineering, University of Nottingham and the China Scholarship Council through a joint PhD studentship awarded to Xiao Liu. This work was also supported by the Engineering and Physical Sciences Research Council, UK [grant number EP/S030786/1].

References

Abu-Bakar, S.H., Muhammad-Sukki, F., Freier, D., Ramirez-Iniguez, R., Mallick, T.K., Munir, A.B., Mohd Yasin, S.H., Abubakar Mas'ud, A., Bani, N.A., 2016. Performance analysis of a solar window incorporating a novel rotationally asymmetrical concentrator. Energy 99, 181–192.
Agathokleous, R.A., Kalogirou, S.A., 2016. Double skin facades (DSF) and building integrated photovoltaics (BIPV): A review of configurations and heat transfer characteristics. Renewable Energy 89, 743–756.
Ahmadi, S., Asim, N., Alghoul, M., Hammadi, F., Saeedfar, K., Ludin, N.A., Zaidi, S.H., Sopian, K., 2014. The role of physical techniques on the preparation of photoanodes for dye sensitized solar cells. Int. J. Photoenergy 2014.
Allen, K., Connelly, K., Rutherford, P., Wu, Y., 2017. Smart Windows—Dynamic Control of Building Energy Performance. Energy Build.
Baig, H., Sellami, N., Chemisana, D., Rosell, J., Mallick, T.K., 2014. Performance analysis of a dielectric based 3D building integrated concentrating photovoltaic system. Sol. Energy 103, 525–540.
Baig, H., Kanda, H., Asiri, A.M., Nazeeruddin, M.K., Mallick, T., 2020. Increasing efficiency of perovskite solar cells using low concentrating photovoltaic systems. Sustainable Energy Fuels.
Brano, V.L., Orioli, A., Ciulla, G., Di Gangi, A., 2010. An improved five-parameter model for photovoltaic modules. Sol. Energy Mater. Sol. Cells 94 (8), 1358–1370.
BS EN 410:2011, 2011. Glass in building – determination of luminous and solar characteristics of glazing. Determination of Characteristics.
Burgers, A., Slooff, L., Kinderman, R., Van Roosmalen, J., 2005. Modelling of luminescent concentrators by ray-tracing. Presented at the 20th European Photovoltaic Solar Energy Conference and Exhibition.
Chen, C.-C., Ting, C.-C., 2013. Photoelectrode fabrication of dye-sensitized nanosolar cells using multiple spray coating technique. Int. J. Photoenergy 2013.
Connelly, K., Wu, Y., Chen, J., Lei, Y., 2016. Design and development of a reflective membrane for a novel Building Integrated Concentrating Photovoltaic (BICPV) 'Smart Window' system. Appl. Energy 182, 331–339.
Connelly, K., Wu, Y., Ma, X., Lei, Y., 2017. Transmittance and Reflectance Studies of Thermotropic Material for a Novel Building Integrated Concentrating Photovoltaic (BICPV)'Smart Window'System. Energies 10 (11), 1889.
Corrado, C., Leow, S.W., Osborn, M., Chan, E., Balaban, B., Carter, S.A., 2013. Optimization of gain and energy conversion efficiency using front-facing photovoltaic cell luminescent solar concentratordesign. Sol. Energy Mater. Sol. Cells 111, 74–81.
Hee, W., Alghoul, M., Bakhtyar, B., Elayeb, O., Shameri, M., Alrubaih, M., Sopian, K., 2015. The role of window glazing on daylighting and energy saving in buildings. Renew. Sustain. Energy Rev. 42, 323–343.
Jensen, H.W., Arvo, J., Dutre, P., Keller, A., Owen, A., Pharr, M., Shirley, P., 2003. Monte Carlo ray tracing. In: ACM SIGGRAPH.
Lambda Research Corporation, 2020. TracePro, Software for Opto-Mechanical Modeling, User's Manual.
Leow, S.W., Corrado, C., Osborn, M., Carter, S.A., 2013. Monte Carlo ray-tracing simulations of luminescent solar concentrators for building integrated photovoltaics. In: SPIE Solar Energy+ Technology. International Society for Optics and Photonics.
Li, X., Liang, Y., Xu, L., 2014. Bidirectional reflectance distribution function based surface modeling of non-Lambertian using intensity data of light detection and ranging. JOSA A 31 (9), 2055–2063.

Li, G., Su, Y., Pei, G., Zhou, H., Yu, X., Ji, J., Riffat, S., 2014. An outdoor experiment of a lens-walled compound parabolic concentrator photovoltaic module on a sunny day in Nottingham. J. Sol. Energy Eng. 136 (2).
Meinardi, F., Bruni, F., Brovelli, S., 2017. Luminescent solar concentrators for building-integrated photovoltaics. Nat. Rev. Mater. 2 (12), 1–9.
Montes, R., Ureña, C., 2012. An overview of BRDF models. University of Grenada, Technical Report LSI-2012. 1.
Nilsson, J., 2005. Optical Design and Characterization of Solar Concentrations for Photovoltaics. Lund University Lund, Sweden.
Nitz, P., Ferber, J., Stangl, R., Wilson, H.R., Wittwer, V., 1998. Simulation of multiply scattering media. Sol. Energy Mater. Sol. Cells 54 (1–4), 297–307.
Norton, B., Eames, P.C., Mallick, T.K., Huang, M.J., McCormack, S.J., Mondol, J.D., Yohanis, Y.G., 2011. Enhancing the performance of building integrated photovoltaics. Sol. Energy 85 (8), 1629–1664.
Nyeinga, K., Okello, D., Nydal, O.J., 2019. A ray tracer model for analysis of solar concentrating systems. J. Energy Southern Afr. 30 (1), 8–20.
Ogbomo, O.O., Amalu, E.H., Ekere, N., Olagbegi, P., 2017. A review of photovoltaic module technologies for increased performance in tropical climate. Renew. Sustain. Energy Rev. 75, 1225–1238.
Paul, D.I., Smyth, M., Zacharopoulos, A., Mondol, J., 2013. The design, fabrication and indoor experimental characterisation of an isolated cell photovoltaic module. Sol. Energy 88, 1–12.
Resch, K., Wallner, G.M., 2009. Thermotropic layers for flat-plate collectors—A review of various concepts for overheating protection with polymeric materials. Sol. Energy Mater. Sol. Cells 93 (1), 119–128.
Rubin, M., Von Rottkay, K., Powles, R., 1998. Window optics. Sol. Energy 62 (3), 149–161.
Sabry, M., 2016. Prismatic TIR (total internal reflection) low-concentration PV (photovoltaics)-integrated façade for low latitudes. Energy 107, 473–481.
Sarmah, N., Mallick, T.K., 2015. Design, fabrication and outdoor performance analysis of a low concentrating photovoltaic system. Sol. Energy 112, 361–372.
Sarmah, N., Richards, B.S., Mallick, T.K., 2011. Evaluation and optimization of the optical performance of low-concentrating dielectric compound parabolic concentrator using ray-tracing methods. Appl. Opt. 50 (19), 3303–3310.
Sarmah, N., Richards, B.S., Mallick, T.K., 2014. Design, development and indoor performance analysis of a low concentrating dielectric photovoltaic module. Sol. Energy 103, 390–401.
Schaepman-Strub, G., Schaepman, M.E., Painter, T.H., Dangel, S., Martonchik, J.V., 2006. Reflectance quantities in optical remote sensing—Definitions and case studies. Remote Sens. Environ. 103 (1), 27–42.
Schneider, J., Seeboth, A., 2001. Natural thermotropic materials for solar switching glazing. Materialwiss. Werkstofftech. 32 (3), 231–237.
Sellami, N., Mallick, T.K., 2013. Optical characterisation and optimisation of a static Window Integrated Concentrating Photovoltaic system. Sol. Energy 91, 273–282.
Sharaf, O.Z., Orhan, M.F., 2015. Concentrated photovoltaic thermal (CPVT) solar collector systems: Part I-Fundamentals, design considerations and current technologies. Renew. Sustain. Energy Rev. 50, 1500–1565.
Simonot, L., 2009. Photometric model of diffuse surfaces described as a distribution of interfaced Lambertian facets. Appl. Opt. 48 (30), 5793–5801.
Skandalos, N., Karamanis, D., 2015. PV glazing technologies. Renew. Sustain. Energy Rev. 49, 306–322.
Su, Y., Pei, G., Riffat, S.B., Huang, H., 2012. A novel lens-walled compound parabolic concentrator for photovoltaic applications. J. Sol. Energy Eng. 134 (2).
Wu, Y., Connelly, K., Liu, Y., Gu, X., Gao, Y., Chen, G.Z., 2016. Smart solar concentrators for building integrated photovoltaic façades. Sol. Energy 133, 111–118.
Xuan, Q., Li, G., Lu, Y., Zhao, B., Zhao, X., Su, Y., Ji, J., Pei, G., 2019. Overall detail comparison for a building integrated concentrating photovoltaic/daylighting system. Energy Build. 199, 415–426.
Zhang, Y., Sun, S., Kang, R., Zhang, J., Zhang, N., Yan, W., Xie, W., Ding, J., Bao, J., Gao, C., 2015. Polymethylmethacrylate-based luminescent solar concentrators with bottom-mounted solar cells. Energy Convers. Manage. 95, 187–192.